JOURNAL OF THERMOPHYSICS AND HEAT TRANSFER
Vol. 11, No. 2, April–June 1997

Coupled Thermal Analysis Method with Application to Metallic Thermal Protection Panels

Dean Kontinos*
NASA Ames Research Center, Moffett Field, California 94035-1000

Metallic thermal protection systems are being considered for next-generation reusable launch vehicles. Experiments and numerical simulations show that heated metallic panels expand from the structure to create a quilt-like flow surface that alters the expected surface heating distribution. To model the thermal response of a metallic panel, this paper presents a two-dimensional boundary element procedure that is loosely coupled to a hypersonic computational fluid dynamics algorithm to solve coupled steady-state and transient heat conduction. First, the flowfield and internal temperature distribution of ceramic wing leading edge in a Mach 15 freestream is computed. Steady-state results are consistent with previous finite difference and finite element calculations. Transient computations show the peak temperature to occur at steady-state conditions. Second, the flowfield and resulting transient heat transfer is computed for convex and concave metallic panels. It is demonstrated that a transient conduction solution for a deformed metallic panel can be approximated by imposing the heat fluxes generated from a deformed surface flow solution onto an undeformed panel.

Nomenclature

C_p = view factor constant
C_T = convective heat transfer coefficient
c = heat capacity
k_s = solid thermal conductivity
n = surface normal
q_{cond} = conductive heat flux
q_{rad} = radiative heat flux
q_w = convective heat flux
$\tilde{T}$ = perturbation temperature
T_r = recovery temperature
T_w = wall temperature
t = time
W = free-space solution
α = thermal diffusivity
Γ = domain surface
ε = emissivity
ρ = solid density
σ = Stefan–Boltzmann constant
τ = time

Subscript
p = source point

Superscript
m = iteration level

Introduction

NEXT-GENERATION reusable launch vehicles are currently being designed to augment the aging Space Shuttle fleet. The thermal protection system (TPS) is critical to vehicle survival in a hypersonic thermal environment. Although TPS design is primarily governed by mission survival, operational costs are an important constraint. For instance, postflight inspection of the shuttle orbiter ceramic tile and gap filler, which are components of the TPS, requires 89 man-hours for the vehicle surface and an additional 1711 man-hours for the recessed regions.[1] Moreover, an average of 60 tiles are replaced. Combined with the in situ repairs, 5982 man-hours are expended to prepare the shuttle for reflight. Including the material expense, the cost of inspection and maintenance of the ceramic tile TPS is over $500,000 per flight. An additional design constraint determining the operating cost of the vehicle is the payload mass fraction. A large payload mass fraction accrues savings over the lifetime of the vehicle. To maximize the payload mass fraction, the TPS must be designed with minimum, yet adequate, margins of safety. Thus, it is critical that the aerothermal environment and the resultant heat transfer into the vehicle structure be predicted with sufficient accuracy throughout the flight envelope.

To reduce the operational costs associated with ceramic TPS, metallic panels are being proposed for use over portions of the vehicle.[2,3] The use of metallic thermal protection panels introduces additional complexities into the heating analysis as compared with ceramic tiles currently in use. Ceramic tiles have a relatively low thermal conductivity, therefore, the time scale of the flowfield and the structural conduction are disparate. Moreover, they are installed with strain isolation pads that insulate the tile from the vehicle structure. In addition, ceramic tiles have a low coefficient of thermal expansion and maintain their shape throughout the trajectory. Because of these characteristics, and excepting configurations where multidimensional conduction is important, analysis of the fluid dynamics and the structural response of the ceramic tiles is effectively decoupled. Metallic panels, on the other hand, are mechanically attached to the structure. The attachments provide conduction and mechanical stress paths. Furthermore, the metallic panels have a higher coefficient of thermal expansion and significant bowing of the panels is anticipated.[2,3] Bowing of the panels creates a quilt-like flow surface that significantly affects the heating distribution.[4,5] Local hot spots form on the windward face of the bowed panel, the magnitude of which is a function of panel orientation, deflection height, and boundary-layer thickness.[4] Also, metals suffer increased heating from catalytic recombination of molecules at the surface. It is possible to coat the metal to form a noncatalytic surface, however, a scratch through the coating may generate a localized region of high heating. If such a defect occurs on the windward side of a bowed panel, the increased heating effect may be compounded. The modeling of these phenomena is essential for

Received Aug. 12, 1996; revision received Nov. 21, 1996; accepted for publication Nov. 25, 1996.

*Research Scientist, Thermosciences Institute, M/S 230-2. Member AIAA.

accurate prediction of the thermal environment; thus, a coupled fluid–structural analysis of the metallic TPS is required.

There has been considerable effort in the coupling of hypersonic computational fluid dynamics (CFD) to in-depth structural conduction.[6–9] Structural dynamic simulations coupled with hypersonic CFD are rare because of the complexity and cost. Nevertheless, Wieting et al.[10] demonstrate an advanced state of development in modeling the coupled fluid–structural system. As part of that research, Thornton and Dechaumphai[11] model the bowing of a steel panel in a Mach 6.6 flowfield. Finite element procedures are used to solve the flowfield, the transient heat conduction, and the thermoelastic expansion of the metallic panel. The work demonstrates both the capability and the need for modeling the coupled system to predict heating rates accurately. Yet, the full integration of the separate finite element modules restricts the freedom in choosing the flow solver. Chemical and thermal nonequilibrium codes in which confidence has been built are more appropriate for the simulation of a re-entry flowfield.

Consistent with the previously mentioned publications, the solution of solid heat conduction and structural deformation is most commonly performed using either finite difference or finite element techniques. Computational tools based on these two methods are well proven and are readily available for coupling with existing CFD codes. A third option, less frequently used in the aerospace community, is the boundary element method (BEM). Li and Kassab[12,13] have solved joint fluid and structural heating efficiently by coupling CFD to a BEM solution of conduction in the body. The advantage of the BEM over a finite difference or finite element formulation is that only the boundary is discretized. As a result, it is naturally coupled with CFD. The boundary element grid is simply the CFD grid at the fluid–surface interface plus additional grid points defining the boundaries of the body. The interior of the domain is not discretized. This is especially advantageous when coupling to CFD because interior values are superfluous; only surface values are required for coupling. Consequently, the BEM is potentially more efficient than finite difference or finite element methods, which require an interior discretization to produce surface conditions. Using the BEM, the temperature can be computed at any desired interior point through contour integrals over the boundary solution. In summary, advantages of the BEM are a reduction of dimensionality, ease of discretization, and efficient coupling with CFD.

The principle drawback of the BEM is its inability to model transient, nonlinear conduction while still maintaining boundary-only discretization (in the steady-state case, Kirchhoff's transform is used to linearize the governing equation[14]). This may be a significant deficiency for modeling metallic panels that have orthotropic, temperature-dependent thermal properties. Yet, there is evidence that using constant thermal properties may produce results sufficient for design purposes. Chen and Milos[6] present a coupled computation of a ceramic wing leading edge in a hypersonic freestream in which the solid thermal conductivity is parametrically varied over a two order of magnitude range. Surprisingly, the resulting change in the surface temperature history is minimal. This result promotes the possibility of finding an effective linear problem that will be sufficient for design cycle use. Furthermore, Kassab and Divo[15] have developed a new BEM to model transient conduction with spatial-dependent thermal properties using a nonsymmetric forcing function; it is an exciting advancement that is very likely to find eventual application toward modeling nonlinear conduction. Until such a time as the BEM is able to model transient nonlinear conduction, the effects of neglecting the temperature variation of the thermal properties in modeling metallic TPS using the BEM must be investigated thoroughly. Nevertheless, the modeling of the heat conduction in metallic panels using the BEM is worthy of pursuit because of the previously mentioned benefits.

The objective of the current research is to model the aerothermodynamic response of a metallic TPS experiencing thermoelastic deformation during entry. To achieve this objective, a chemically reacting, nonequilibrium, two-dimensional, Navier–Stokes flow solver is coupled to the BEM solution of the transient heat conduction within the metallic panel. The details of the solution and coupling procedure are presented in the next section. Then, the fluid–solid coupling procedure is tested through the computation of the heat transfer to a ceramic wing leading edge in hypersonic flight; this configuration has been simulated by previous researchers. Finally, the calculation of the heat conduction through a bowed metallic panel on the windward side of generic nose–body configuration is presented. The simulation tests coupling procedures applicable for modeling the heat conduction through a thermoelastically bowing panel.

Procedure

The analysis of the heating environment and solid conductive response is performed using two modules. The first is a hypersonic CFD solver for the prediction of the flowfield, and the second module uses the BEM to solve the steady-state and time-dependent heat conduction through the body. The modules are coupled through a surface energy balance boundary condition. The details of the CFD flow solver, the conduction codes, and the coupling of the two are described in this section.

CFD

The hypersonic, chemically reacting flowfield is computed using the GIANTS program of Candler[16] as modified by Olynick et al.[17] The algorithm solves the Navier–Stokes equations in fully conservative finite volume form. The fluxes are discretized in an upwind manner to second-order accuracy in space, and the equations are solved using line Gauss–Seidel relaxation. For the solutions presented in this paper, the pertinent physical models are the following: finite rate chemistry, five-species air (N_2, O_2, NO, N, and O), two-temperature energy model (translation–rotation and vibration), bifurcation model for species diffusion,[17] and surface catalysis consistent with the bifurcation diffusion model. This program has been used extensively and is aptly described in Refs. 16 and 17. Additional validation of the program is given by Olynick and Henline.[8]

BEM for Steady-State and Transient Heat Conduction

The heat conduction through the interior of the body is solved using the BEM. Readers unfamiliar with the BEM should consult textbooks on the subject such as Brebbia et al.[18] or Gipson.[19] The heart of the BEM is the boundary integral equation that can be derived from either a weighted residual approach or reciprocity considerations. In either case, the boundary integral equation for linear, transient, heat conduction is given by

$$C_p\tilde{T}_p + \alpha \int_\tau \int_\Gamma \tilde{T}\,\frac{\partial W}{\partial n}\,\mathrm{d}\Gamma\,\mathrm{d}\tau - \alpha \int_\tau \int_\Gamma W\,\frac{\partial \tilde{T}}{\partial n}\,\mathrm{d}\Gamma\,\mathrm{d}\tau = 0 \qquad (1)$$

where $\mathrm{d}\tilde{T}/\mathrm{d}n$ is the temperature gradient, referenced to an initial steady-state temperature distribution, and C_p is a multiplicative constant that is a function of the local view factor into the domain. Equation (1) expresses the temperature at a given point as a function of two integral transforms; the first is the integral transform over the boundary and time of the temperature with the gradient of the free-space solution as kernel, and the second is the transform of the temperature gradient with the free-space solution as kernel. The integral transforms are computed by approximating the surface as a sum of elements similar to the finite element method. Like the finite element method, there is freedom in selecting the order of the shape function determining the boundary shape and the inter-

polation function approximating the dependent variable distribution. Thus, Eq. (1) is the basis for a numerical procedure where the nodal points are on the boundary only. By taking the point p to be each node of the boundary in turn, a system of linear equations is formed. The unknowns are the boundary temperature or temperature gradient depending on the type of boundary condition. Solution of the system of equations yields the value of the temperature and temperature gradient along the boundary. The temperature at any point on the interior is found by reapplication of Eq. (1). Since the boundary data are known from the solution of the aforementioned linear system, the interior values are found by computing the contour integral around the boundary. Once the boundary values are known, any subset of the interior can be calculated to any desired resolution. For instance, the interior solution is not required to couple a CFD solution; only the surface conditions need to be known.

The steady-state and transient BEM algorithms used in this study are given by Kontinos[20] and are shown to be second-order accurate in space and time. They are designed for efficient coupling with CFD discretizations and feature piecewise linear elements for exact mating with the flowfield grid. The features of the algorithms are listed here, whereas the complete details are given in Ref. 20. The steady-state algorithm employs the fundamental solution approach; the integration kernels are computed analytically based on linear shape functions, linear elements, and variably offset nodal points. The transient algorithm employs the transient fundamental solution; the temporal integration is performed analytically and the nonsingular spatial integration is performed numerically using Gaussian integration. The boundary-only character of the algorithm is maintained by integrating the influence coefficients from initial time.

Fluid–Structural Coupling

Equations for generalized fluid–structure surface thermochemistry modeling are presented by Milos and Rasky.[21] In this study, the fluid dynamic solution is loosely coupled to the BEM conduction solution through the surface energy balance, given by

$$q_w = q_{\text{cond}} + q_{\text{rad}} \tag{2}$$

where q_w is generated by the flowfield and includes fluid conduction, diffusion, and chemical recombination terms; q_{cond} is the conduction into the solid material; and q_{rad} is the radiation away from the surface. An efficient procedure to iterate between the CFD and conduction solutions using Eq. (2) is given by Chen and Milos[6] and Imlay et al.[22] In this method, the convergence of the fluid and structural solution is accelerated by relating T_w to the convective heat flux through C_T, which is defined as

$$C_T = q_w/(T_r - T_w) \tag{3}$$

For hypersonic flow, T_r is approximated as the freestream kinetic enthalpy divided by the coefficient of heat at constant pressure. Substitution of Eq. (3) into Eq. (2) yields a nonlinear boundary condition of the third kind, which is solved in the conduction module. With the radiation and conduction terms written explicitly in terms of surface quantities, the expression becomes

$$C_T T_w + k_s \frac{\partial T}{\partial n} = C_T T_r - \varepsilon\sigma T_w^4 \tag{4}$$

where $\partial T/\partial n$ is the temperature gradient interior of the solid and normal to the surface. The fluid dynamics and the solid conduction are coupled at select times in the trajectory. These times are named anchor points. Between anchor points, the heat transfer coefficient is assumed to vary linearly. Thus, in Eq. (4), C_T is a piecewise linear function of time.

The nonlinear boundary condition given by Eq. (4) cannot be solved explicitly using the BEM. Consequently, a subiteration technique is constructed by lagging the wall temperature (note: this solution process is termed subiterative to distinguish it from the global iteration between the fluid dynamic and solid conduction solutions). The subiterative expression is given by

$$[C_T(t) + \varepsilon\sigma T_w^{m^3}]T_w^{m+1} + k_s \frac{\partial T^{m+1}}{\partial n} = C_T(t)T_r \tag{5}$$

where the temporal dependence of C_T is explicitly written for clarity. At each subiteration, the recent wall temperature values are used to update the coefficient $\varepsilon\sigma T_w^3$. The subiteration is complete when the nonlinear boundary condition is satisfied within a set tolerance. In practice, the wall temperature values are underrelaxed and strict convergence ($\|T_w^{m+1} - T_w^m\| < 10^{-6}$) is achieved in four to seven iterations per time step.

To start the global iteration process, the convective heat transfer must be prescribed. For a re-entry trajectory the initial heat transfer is typically assumed to be zero. For an ascent trajectory, an equilibrium condition is assumed and the flowfield is computed using a constant wall temperature given by the structure temperature. This results in q_w, and hence, C_T, at time zero. Then, an initial guess for the wall temperature is generated for the first anchor point by solving the flowfield using a radiative equilibrium condition, i.e., $q_{\text{cond}} = 0$. The resultant convective heat transfer is used to compute C_T, which is then assumed to vary linearly in time. The expression for C_T is substituted into Eq. (5), and the conduction equation is integrated in time up to the first anchor point. The conduction solution yields the wall temperature and conductive heat flux satisfying the surface energy balance. The resultant wall temperature distribution is fed back into the CFD module as a constant wall temperature condition upon which the flowfield is recomputed to obtain improved values of C_T. The iteration is repeated by running the conduction module with the updated C_T values. The procedure is continued to convergence.

Results

To test the coupling procedures previously described, the computation of a ceramic wing leading edge in a hypersonic freestream is presented. Results of computations using both the steady-state and transient conduction codes coupled to the flowfield solution are presented. Then, the calculation of the transient heat conduction through a homogeneous, bowed, metallic panel located on the windward side of a generic nose–body configuration is presented. This final case tests coupling procedures applicable for modeling the thermoelastic deformation of the panel.

Wing Leading-Edge—Steady-State Conduction

The conduction modules (steady state and transient) and the coupling procedures are tested through the computation of a ceramic wing leading edge. This type of geometry is currently being studied for use in advanced hypersonic flight vehicle concepts. This is the same case computed by Chen and Milos[6] and Molvik et al.[7] The geometry is a 0.254-cm-radius leading edge blended into a 5-deg ramp surface. The length of the domain is 8.1 cm. The flowfield is at cruise conditions of Mach 15 at an altitude of 30.48 km. The computational grid is 80 points in the streamwise direction and 55 points normal to the body. Only half of the flowfield and body is modeled since the angle of attack is zero and symmetry exists about the axis.

The wing is composed of advanced diboride ceramic–matrix composite.[23] The following material properties are used: k_s = 67.5 W/m-K, ρ = 5238.09 kg/m^3, c = 808 J/kg-K, and ε = 0.6. These material properties yield a thermal diffusivity of 1.5949×10^{-5} m^2/s. The boundary element grid is the same as the CFD grid along the body surface with 24 additional elements to define the wing thickness. The grid points along

the symmetry line are clustered toward the nose. The surface energy balance of Eq. (4) is solved on the wing surface and a zero gradient condition is imposed on both the centerline (symmetry) and the downstream boundary (adiabatic).

The calculation of the coupled flowfield and solid conduction is performed using both the steady-state and transient conduction modules. First, the steady-state results are shown. The case is computed with both noncatalytic and fully catalytic surface chemistry to bound the possible temperature range of the wing configuration. The conduction results are shown in Fig. 1 along with temperature profiles generated from the radiative equilibrium assumption. The addition of the conduction modeling reduces the stagnation temperature by 680 K in the catalytic case, and 706 K in the noncatalytic case. Physically, the heat generated at the nose is conducted through the body and back into the flowfield starting near the ramp juncture and continuing downstream. Thus, one sees a reduction of the stagnation temperature and an increase in the ramp temperature as compared to the radiative equilibrium solution. The stagnation temperature of all four solutions exceeds the melt limit of the material, which is approximately 3000 K.

The stagnation temperature of the fully catalytic radiative equilibrium solution is 700 K higher than that reported by Chen and Milos[6] and Molvik et al.[7] This is because of different modeling of the surface thermochemistry. In the previously mentioned results, chemical equilibrium was used to simulate a fully catalytic surface. This assumption is common and applicable for cold wall conditions. In this instance, however, the wall temperature is higher than the dissociation temperature of oxygen and full recombination does not occur under equilibrium conditions. Since catalytic recombination releases the energy of dissociation into the wall and the results reported here are for a complete recombination of nitrogen and oxygen, the wall temperature is greater than that produced by the equilibrium assumption. As a measure of the potential for recombinative heating, flowfield contours of the degree of dissociation of oxygen are shown in Fig. 2 for the fully catalytic condition. This scalar field is computed as the ratio of the density of monatomic oxygen to the sum of the monatomic and diatomic oxygen densities. This definition does not account for the amount of oxygen present in the flowfield as NO, since the catalytic condition forces the recombination of free monatomic oxygen and NO does not participate in the catalytic reactions. The dissociation is nearly complete in the stagnation region and significant amounts exist along the length of the body. Of course, the real measure of the recombinative heating effect is observed in the boundary layer. Nevertheless, Fig. 2 shows that the oxygen does indeed recombine at the wall. Differences in the stagnation temperatures between the current results and those of Refs. 6 and 7 may also be attributable in part to discretization and numerical damping differences.

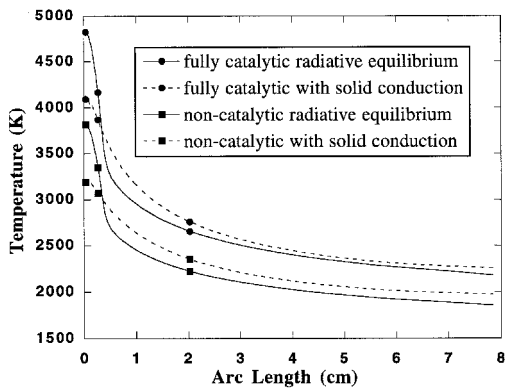

Fig. 1 Wing leading-edge surface temperature distributions.

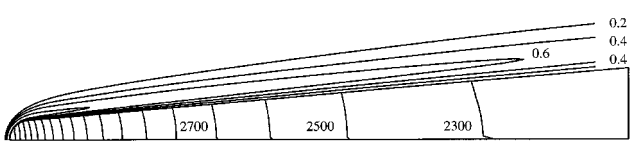

Fig. 2 Degree of oxygen dissociation contours in wing leading-edge flowfield along with body temperature contours.

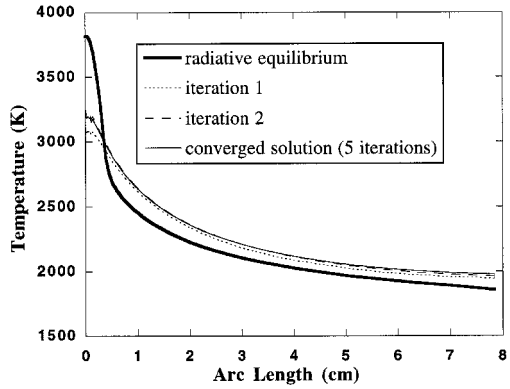

Fig. 3 Wing leading-edge surface temperature distribution convergence history.

Also shown in Fig. 2 are steady-state temperature contours in the interior of the wing generated by the conduction code. A discontinuity in the temperature contours exists at the symmetry line because of stretching of the boundary elements and an inconsistency in postprocessing the data. In Fig. 2, the interior temperature is computed through the boundary integral equation whereas, for convenience, the boundary temperature is the result of a linear fit of the nodal data along the boundary element. The boundary elements are stretched along the symmetry line, and consequently, the linear fit is inconsistent with the nonlinear temperature distribution resulting from the boundary integral equation. The discontinuity can be removed by either increasing the number of boundary elements along the centerline or by computing the boundary temperatures using the boundary integral equation, however, this functionality has not been implemented. The boundary element resolution at the fluid–solid interface is sufficient to produce smooth contours using a linear fit of the surface data.

The performance of the coupling procedure is presented in Fig. 3. Shown is the radiative equilibrium solution of the noncatalytic surface along with the solution of the solid conduction after the first, second, and final iteration of the surface energy balance. The converged solution is obtained after five iterations, when the changes in the surface temperature are less than 1 deg. This is a fairly stringent convergence requirement; for engineering purposes, the surface conditions can be taken after the second iteration. The results here verify those reported by Chen and Milos.[6] Indeed, the results reported here are for different flow and conduction codes, which shows the algorithm independence of the iteration procedure.

Wing Leading-Edge—Transient Conduction

A transient simulation for the wing leading edge is also constructed. Since cold wall temperatures impede convergence of the reacting gas CFD solution, the initial temperature throughout the wing is set to a uniform temperature of 1000 K; this is deemed sufficient for the purpose of testing the transient conduction code. The transient heating of the wing is simulated from the 1000 K initial condition in the Mach 15 flowfield. This trajectory might represent a wind-tunnel test where a preheated model is injected into the freestream of the tunnel. For the present computational simulation, the wall is assumed to be noncatalytic.

The computational characteristics of the boundary element solution are investigated. The first 10 s of the transient response is computed for four combinations of time step and anchor point distribution. Recall that an anchor point is defined

as a point in the computation where a flowfield solution is generated. Between anchor points, C_T is linearly interpolated in time providing the boundary condition for integration time steps smaller than the anchor point distribution. The resultant stagnation point temperatures of the four solutions are plotted in Fig. 4.

A fine resolution case is computed with an anchor point every 1 s and a time step of 0.2 s. The heating of the nose seems well represented by this calculation. The stagnation point reaches 98% of its steady-state value within the first 10 s. This result is consistent with a 0.4-s characteristic time scale calculated by the square of the nose radius divided by the thermal diffusivity.

The 10-s computation is performed again, but with a time step of 1 s, which results in one time step per anchor point. The result is shown in Fig. 4. Assuming that the original computation is more accurate, the increase of the time step does not reduce the accuracy of the computation; the two solutions differ by 2.2% at 1 s and then differ by less than 0.3% at the remaining anchor points. Nevertheless, the resolution of the solution is decreased, which is evident in the first second where a linear fit in time underpredicts the temperature from the original solution. If the temperature or temperature gradient are approximately linear over a given time step, then subdividing the time interval by taking smaller time steps does not necessarily improve the accuracy of the solution. This is because the boundary element algorithm incorporates linear shape functions over time to approximate the solution; the accuracy is determined by how well the shape functions model the physical data over time and space, and how accurately the integration of these shape functions is performed. Therefore, smaller time steps do not improve the accuracy if the solution is linear in time.

Also investigated in the first 10 s is the anchor point spacing that is governed by the surface energy balance relation. The spacing requirements are that C_T is accurately represented as a linear function of time. Figure 5 shows C_T at the stagnation point, near the ramp juncture, and near the downstream boundary as a function of time. Only the nose region diverges markedly from a linear distribution, but it is only over the first 2 to 3 s. Thus, it is anticipated that large spacing of the anchor points will still resolve the temporal C_T distribution. This hypothesis is tested by computing the 10-s history with a time step of 0.2 s and an anchor point every 5 s. The stagnation point temperatures are shown in Fig. 4. Within the first 5 s, the calculation overpredicts the stagnation temperature of the original fine resolution case. This is consistent with a linear fit of the C_T distribution between 0–5 s (see Fig. 5); the values of C_T are higher than the fine resolution case over the 5-s interval, consequently, the integrated heat rate increases, thereby increasing the temperature. Over the next interval of 5–10 s, the C_T distribution is linear and the increase in anchor point spacing does not affect the solution. Surprisingly, the solution at the 5-s anchor point is within 1% of the original high-resolution solution. Indeed, the temperature profile has a slope discontinuity in time as if the solution is tied to the anchor point.

To investigate this further, a fourth 10-s computation is performed with both a time step and anchor point interval of 5 s. The result for the stagnation line is shown in Fig. 4. The solutions at the 5- and 10-s anchor points are still within 1.2% to the original high-resolution computation. Thus, in the first 10 s, the solution at the anchor point is fairly insensitive to the anchor point spacing and the time step. This characteristic has yet to be fully explained and is still under investigation.

Based on the previous analysis, the wing transient temperature response is calculated with a time step of 5 s and an anchor point every 10 s. The results are shown every 30 s and are plotted in Fig. 6. The boundary element algorithm predicts the wing to reach its steady-state distribution in approximately 2 min. This is on the order of the characteristic time scale based on the square of the length of the body divided by the thermal diffusivity. The final steady-state surface temperature distribution predicted by the transient code is the same as that produced by the steady-state code. It is also important to note that the transient solution approaches the steady state from below, that is, the transient temperature does not exceed the steady-state temperature.

Finally, as an example of the resolution achieved with the current high-fidelity analysis, the location and time in which heat begins to conduct into the flowfield are determined. Figure 7 shows the conductive heat flux along the surface at times of 1 and 7 s along with the steady-state values. At 1 s, the radiative heat flux is small because the surface temperature is low, thus, the conductive heat flux is high to balance the convective heat flux. As the surface temperature increases, the radiative flux increases and the convective flux decreases. Between 6 and 7 s, at approximately 0.4 cm in arc length (this location is at the ramp juncture), a true radiative equilibrium con-

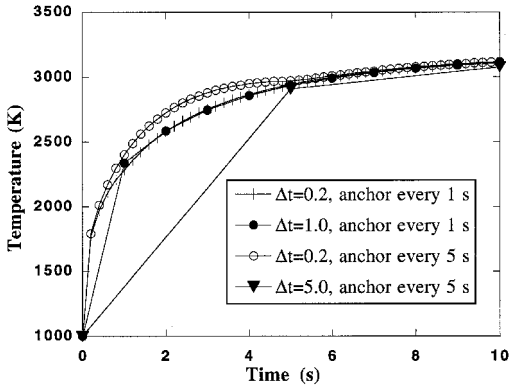

Fig. 4 Wing leading-edge stagnation point temperature history for varying time step and anchor point distributions.

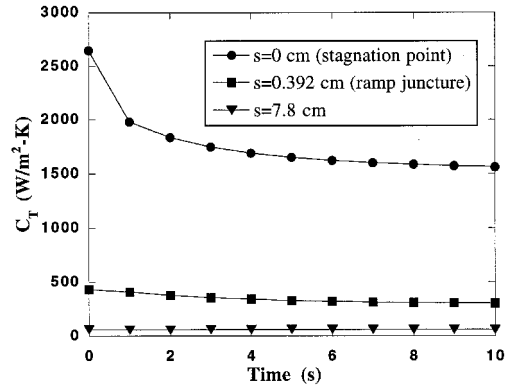

Fig. 5 Wing leading-edge heat transfer coefficient history.

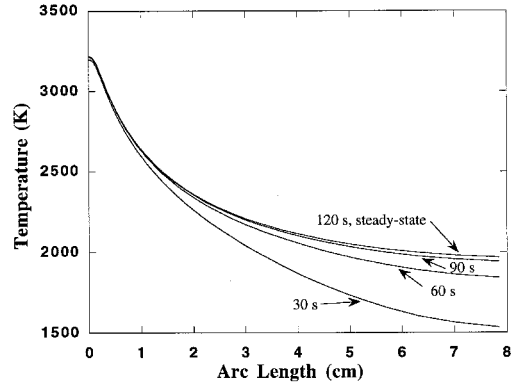

Fig. 6 Wing leading-edge surface temperature distributions at 30, 60, 90, and 120 s.

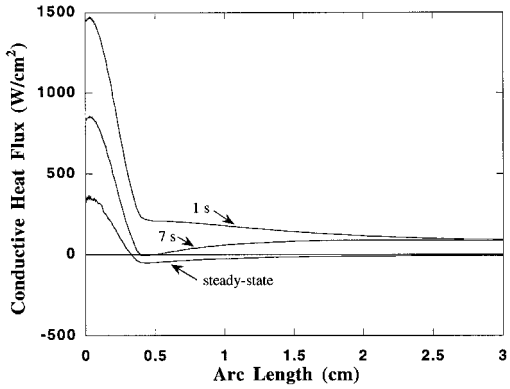

Fig. 7 Wing leading-edge conductive heat flux at 1 s, 7 s, and steady state.

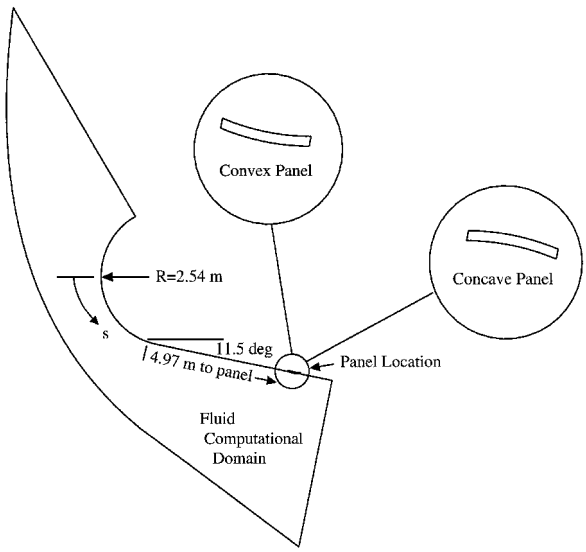

Fig. 8 Schematic of flowfield geometry and location of bowed metallic panel.

dition exists, that is, the convective flux is exactly balanced by the radiative flux and the conductive flux is zero. In the steady state, heat is absorbed by the body forward of the juncture and is conducted into the flowfield downstream of the juncture.

Bowed Metallic Panel

The final test of the transient module is the computation of a homogeneous metallic panel on the windward side of a generic re-entry lifting body configuration. In addition to modeling the gross effects of a bowed metallic panel, this calculation tests coupling procedures applicable for modeling the transient conduction through the metallic panel using the BEM in conjunction with the solution of the thermoelastic response. It is assumed that a surface deflection is obtainable given the temperature distribution within the panel. This can result from analytic expressions from plate theory, BEM solution of the linear elastic equations, or a finite element solution. In either case, the temperature distribution from the transient conduction calculation is considered sufficient to obtain the structural displacement. The displacement field yields a new surface shape that alters the flowfield solution. An efficient procedure to account for the surface deformation is to recompute the flowfield with the updated surface definition coupled with the temperature boundary condition from the conduction module. The convective heat flux generated from the updated surface shape is used as the boundary condition for the transient heat computation on the original undeformed panel. In other words, the domain used for the heat conduction module remains fixed at the initial undeformed state. This assumption simplifies the coupling process by eliminating the time dependency of the structural domain when solving the transient heat conduction. In this section the coupling procedure is tested through the computation of a single, homogeneous, metallic panel located on the windward side of a nose–body configuration. A deformed panel shape is assumed and the transient thermal response of the panel is computed using two independent procedures. First, the thermal conduction through the deformed panel is computed. Second, the flowfield surface conditions generated from the deformed surface shape are imposed onto the undeformed panel. These two solutions are shown to be nearly identical for both a convex and a concave panel deformation.

The geometry is a 2.54-m-radius circular nose with a ramp of 11.5 deg, as shown schematically in Fig. 8. The panel is 0.4572 m long, 0.0508 m thick, and located 4.97 m along the ramp downstream of the nose juncture. The following constant material properties, which roughly correspond to the in-depth direction of a honeycomb panel with Cerachrome[2] insulation at 1000 K, are used for the analysis: k_s = 0.433 W/m-K, ρ = 96.11 kg/m^3, c = 1222.6 J/kg-K, and ε = 0.85. The thermal diffusivity is 3.6831×10^{-6} m^2/s; over the range of 280–1000 K, the actual temperature-dependent thermal diffusivity varies 33%. The body is assumed to be composed of a carbon tile thermal protectant. The surface catalysis is computed using the reaction cured glass (RCG) surface kinetics incorporated by Olynick and Henline,[8] with rate coefficient curve fits given by Stewart et al.[24] The emissivity is 0.85. The metallic panel catalysis is computed using the RCG kinetics as well. This assumption is not strictly accurate, however, the purpose of the computation is to compare the conduction solutions computed by the deformed and undeformed configurations. It has been shown that discontinuous changes in wall catalysis can cause disturbances in the wall temperature distribution.[8,25] To isolate the bowing and conduction effects, this analysis excludes this phenomena by maintaining a single catalysis model along the surface.

The re-entry trajectory is given by the three anchor points displayed in Table 1. The boundary layer is assumed to remain laminar throughout the trajectory. In actual flight, transition to turbulence may be triggered by surface waviness, surface roughness, and interpanel mold line discontinuities, however, a transition criteria has yet to be established and the issue is not addressed in this analysis. The angle of attack is 40 deg throughout the trajectory. The initial temperature of the panel is assumed to be 280 K. The time step of the conduction module is 50 s, which reasonably resolves the temperature history using a temporally linear shape function in the BEM. The flowfield grid is 78 points streamwise and 55 points normal to the body. There are 11 points (10 elements) on the panel surface. The remaining panel is composed of 20 additional elements. The panel is insulated on the sides and at the back face.

The flowfield and transient history of the panel is computed for an undeformed panel throughout the flight trajectory. The surface temperature and heat flux distributions at the three trajectory anchor points are plotted in Fig. 9. In Figs. 9–11 the ordinate is the surface arc length with zero being the centerline at 0-deg angle of attack (see Fig. 8). The panel is located from arc length 8.45 to 8.94 m. Conduction is modeled through the panel only. The remaining surface is computed using a radia-

Table 1 Flight trajectory for bowed metallic panel case

Flight time, s	Altitude, km	Mach number
1000	85.34	25
1500	73.15	22
2000	47.24	9

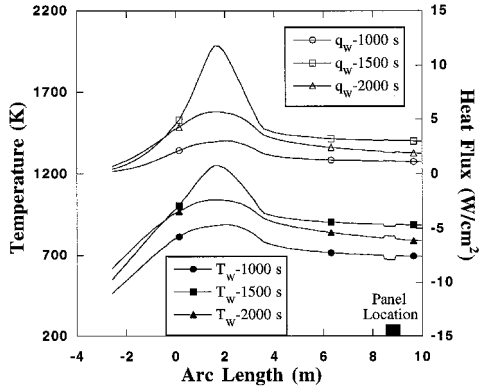

Fig. 9 Surface temperature distribution with undeformed panel.

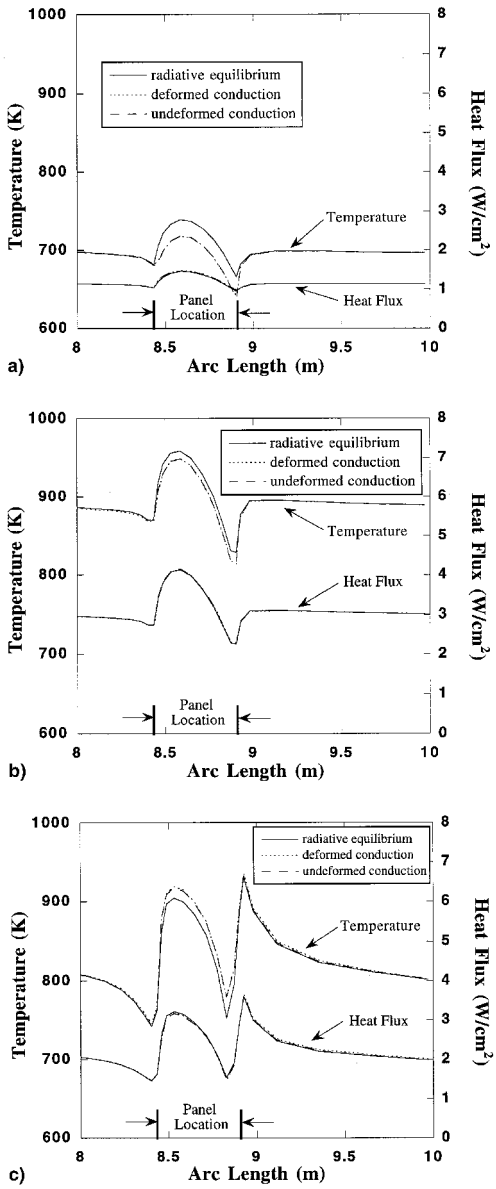

Fig. 10 Surface temperature distribution with convex panel: a) 1000, b) 1500, and c) 2000 s.

tive equilibrium condition. Therefore at the 1000-s anchor point location, the panel surface temperature is lower than the surrounding surface temperature because of finite rate conduction. The same reduction in temperature is seen at 1500 s, which is the peak heating time for this trajectory. At 2000 s the surface temperature of the panel is greater than that of

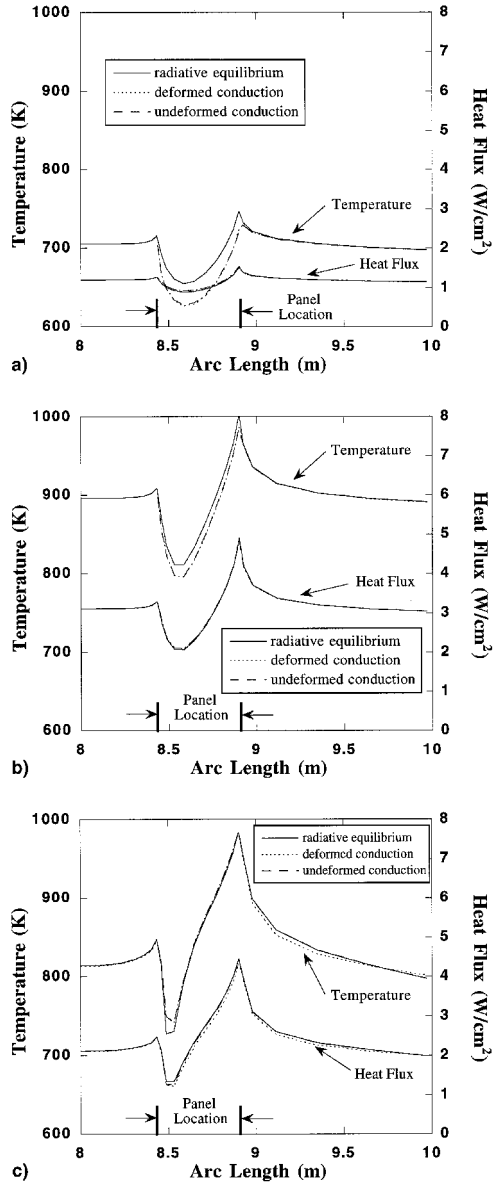

Fig. 11 Surface temperature distribution with concave panel: a) 1000, b) 1500, and c) 2000 s.

upstream and downstream carbon tiles. At this time, the heat absorbed by the panel earlier in the flight is being transferred back into the flowfield. Of course, the surrounding carbon tiles also conduct heat at a finite rate and, therefore, the discontinuity of the surface temperature at the panel is exaggerated. Moreover, for simplicity, the surface material downstream of the panel reverts back to carbon tile. An actual flight vehicle will have a series of metallic panels. Nevertheless, this case is adequate for use as a baseline for comparison with the bowed surface configurations.

Next, two simulations are computed with a convex- and a concave-bowed panel surface. The surface is prescribed to be circular with a maximum deflection distance of 0.04572 m to yield a bow height to panel length ratio of 0.1. The deformed panel shapes are shown in Fig. 8. Recall that the purpose of this computation is to compare the conduction solution of the deformed to undeformed panels. The convex and concave configurations are not predictive of the actual deformed surface shape, but are exaggerated to test the coupled fluid-thermal solution strategy; preliminary estimates for bow height to panel length ratios are in the range of 0.01–0.03.

The surface temperature and heat flux distributions on the convex panel are shown in Fig. 10 at the three trajectory

points. Three solutions are plotted: 1) a radiative equilibrium condition, 2) a solution coupled with the transient conduction module using the deformed body shape, and 3) a conduction solution with the flowfield generated by the bowed surface imposed on the undeformed panel. At 1000 and 1500 s, the convex bow causes the temperature to rise on the upstream side of the protruding surface; then the temperature decreases as the flow expands around the downstream side. The addition of the conduction modeling decreases the panel surface temperature as compared to the radiative equilibrium solution. The convective heat flux is mostly unaffected by the addition of conduction. The radiative heat flux, and hence, the temperature, decreases to compensate for the conduction. This result is consistent with those presented in Fig. 9. More importantly, the surface temperature distribution of the deformed panel and the undeformed panel with the imposed surface conditions are nearly identical; both solutions are iterated independently. At 2000 s, the convex deformation causes the flow to separate on the downstream side of the protuberance; in the reattachment zone, the temperature increases to values on the order of the stagnation point. Consistent with Fig. 9, the addition of the conduction modeling increases the panel surface temperature. The deformed and undeformed surface temperatures are nearly identical at this anchor point as well.

In Fig. 11 the surface temperature and heat flux profiles for the concave deformation are shown. The concave surface produces flow disturbances that are more severe than the convex deformation because the flow is accelerated before it is turned back on the downstream side of the panel. The addition of the conduction modeling decreases the panel surface temperatures at 1000 and 1500 s, and increases them at 2000 s. For the concave surface shape, the flow is separated at both 1500 and 2000 s. Moreover, the disturbances caused by the separation overwhelm the effect of the conduction, and little difference between radiative equilibrium and conduction solutions are seen. As with the convex surface, it is seen that the conduction solution is not altered by imposing the flowfield heat fluxes generated by the deformation onto the original undeformed panel.

Conclusions

To model the thermal response of a metallic thermal protection panel, a boundary element procedure has been developed to compute steady-state and transient heat conduction for constant material properties. The boundary element codes are loosely coupled to a hypersonic, reacting gas flow solver to compute the steady-state and transient conductive heating of a wing leading edge in a Mach 15 flowfield. The procedure developed by Chen and Milos[6] is shown to be applicable in coupling the boundary element codes to the CFD code. The modeling of the solid conduction reduces the stagnation temperature on the wing as compared to the common radiative equilibrium assumption. The results using the BEM codes are consistent with previous results using finite difference and finite element codes. Transient computations show that the maximum temperature in the body occurs at steady state. Also, the transient heating solutions of a convex and a concave bowed metallic panel on the windward side of a nose–body configuration are presented. It is shown that two independently iterated transient conduction solutions produce nearly identical surface temperatures. The first solution is computed using the actual deformed panel shape; the second solution is generated by imposing the flowfield heat flux computed using the deformed surface shape onto the original undeformed panel shape. This result supports the validity of simplifying the thermoelastic coupling process by eliminating the time dependency of the structural domain when solving the transient heat conduction. Finally, the boundary element procedure is shown to be an effective method for computing coupled fluid/structural heat conduction.

Acknowledgments

This research was performed while the author was a Research Associate working under a grant from the National Research Council under the supervision of Thomas Edwards of NASA Ames Research Center. Part of this work was performed under NASA Contract NAS2-14031 to Eloret. The author would like to thank David Olynick of NASA Ames Research Center for his assistance with the GIANTS code, Alain Kassab of the University of Central Florida for his patience and commitment in instructing the author in boundary element techniques, and Y.-K. Chen of Thermosciences Institute for discussions on coupling procedures.

References

[1]Anon., "Advanced Manned Launch System Reusable Cryogenic Tank Design Task 5," Rockwell Space System Div., National Academy of Sciences, 18975, Downey, CA, Sept. 1993.

[2]Gorton, M. P., Shidler, J. L., and Webb, G. L., "Static and Aerothermal Tests of a Superalloy Honeycomb Prepackaged Thermal Protection System," NASA TP-3257, March 1993.

[3]Avery, D. E., Shideler, J. L., and Stuckey, R. N., "Thermal and Aerothermal Performance of a Titanium Multiwall Thermal Protection System," NASA TP-1961, Dec. 1981.

[4]Olsen, G. C., and Smith, R. E., "Aerothermal Loads Analysis for High Speed Flow over a Quilted Surface Configuration," AIAA Paper 84-1630, June 1984.

[5]Olsen, G. C., and Smith, R. E., "Analysis of Aerothermal Loads on Spherical Dome Protuberances," *AIAA Journal*, Vol. 23, No. 5, 1985, pp. 650–656.

[6]Chen, Y.-K., and Milos, F. S., "Solution Strategy for Thermal Response of Nonablating Thermal Protection Systems at Hypersonic Speeds," AIAA Paper 96-0615, Jan. 1996.

[7]Molvik, G. A., Milos, F. S., Chen, Y.-K., and Squire, T. H., "Computation of High Speed Flow Fields with Multidimensional Heat Conduction," AIAA Paper 95-2116, June 1995.

[8]Olynick, D. R., and Henline, W. D., "Navier-Stokes Heating Calculations for Benchmark Thermal Protection System Sizing," *Journal of Spacecraft and Rockets*, Vol. 33, No. 6, 1996, pp. 807–814.

[9]Yamamoto, Y., and Yoshioka, M., "CFD and FEM Coupling Analysis of Orex Aerothermodynamic Flight Data," AIAA Paper 95-2087, June 1995.

[10]Weiting, A. R., Dechaumphai, P., Bey, K. S., Thornton, E. A., and Morgan, K., "Application of Integrated Fluid-Thermal-Structural Analysis Methods," NASA TM-100625, May 1988.

[11]Thornton, E. A., and Dechaumphai, P., "Coupled Flow, Thermal, and Structural Analysis of Aerodynamically Heated Panels," *Journal of Aircraft*, Vol. 25, No. 11, 1988, pp. 1052–1059.

[12]Li, H., and Kassab, A. J., "A Coupled FVM/BEM Approach to Conjugate Heat Transfer in Turbine Blades," AIAA Paper 94-1981, June 1994.

[13]Li, H., and Kassab, A. J., "Numerical Prediction of Fluid Flow and Heat Transfer in Turbine Blades with Internal Cooling," AIAA Paper 94-2933, June 1994.

[14]Carslaw, H. S., and Jaeger, J. C., *Conduction of Heat in Solids*, Oxford Univ. Press, Oxford, England, UK, 1959.

[15]Kassab, A. J., and Divo, E., "A Generalized Boundary Integral Equation for Isotropic Heat Conduction Problems with Spatially Varying Thermal Conductivity," *Engineering Analysis* (to be published).

[16]Candler, G. V., "The Computation of Weakly Ionized Hypersonic Flows in Chemical Nonequilibrium," Ph.D. Dissertation, Stanford Univ., Stanford, CA, June 1988.

[17]Olynick, D. R., Henline, W. D., Chamber, L. H., and Candler, G. V., "Comparison of Coupled Radiative Flow Solutions with Project Fire II Flight Data," *Journal of Thermophysics and Heat Transfer*, Vol. 9, No. 4, 1995, pp. 586–594.

[18]Brebbia, C. A., Telles, J. C. F., and Wrobel, L. C., *Boundary Element Techniques—Theory and Applications in Engineering*, Springer–Verlag, Berlin, 1984.

[19]Gipson, G. S., "Boundary Element Fundamentals—Basic Concepts and Recent Developments in the Poisson Equation," *Topics in Engineering*, edited by C. A. Brebbia and J. J. Conner, Vol. 2, Computational Mechanics Publications, Boston, MA, 1987.

[20]Kontinos, D. A., "Steady-State and Transient Boundary Element Methods for Coupled Heat Conduction," NASA TM-110427, Jan. 1997.

[21]Milos, F. S., and Rasky, D. J., "A Review of Numerical Proce-

dures for Computational Surface Thermochemistry," *Journal of Thermophysics and Heat Transfer*, Vol. 8, No. 1, 1994, pp. 24–34.

[22]Imlay, S. T., Soetrisno, M., and Roberts, D. W., "Coupled Flow and Heat Transfer Analysis Using Structured-Unstructured Grids," AIAA Paper 96-0622, Jan. 1996.

[23]Bull, J. D., and Rasky, D. J., "Stability Characterization of Diboride Composites Under High Velocity Atmospheric Flight Conditions," *Proceedings of the 24th International SAMPE Technical Conference*, SAMPE, Covina, CA, 1992 (Paper T-1092).

[24]Stewart, D. A., Rakich, J. V., and Chen, Y.-K., "Flight Experiment Demonstrating the Effect of Surface Catalysis on the Heating Distribution over the Space Shuttle Heat Shield," *Orbiter Experiments (OEX) Aerothermodynamics Symposium*, edited by D. A. Throckmorton, Pt. 2, 1993, pp. 677–702 (NASA CP-3248).

[25]Palmer, G., Henline, W. D., Olynick, D. R., and Milos, F. S., "A Heating Analysis and Thermal Protection System Sizing of a Lifting Body Single-Stage-to-Orbit Vehicle," AIAA Paper 95-2080, June 1995.